JOURNAL OF AIRCRAFT
Vol. 29, No. 5, Sept.–Oct. 1992

Multidisciplinary Optimization of Aeroservoelastic Systems Using Reduced-Size Models

Mordechay Karpel*
Technion—Israel Institute of Technology, Haifa 32000, Israel

Efficient analytical and computational tools for simultaneous optimal design of the structural and control components of aeroservoelastic systems are presented. The optimization objective is to achieve aircraft performance requirements and sufficient flutter and control stability margins with a minimal weight penalty and without violating the design constraints. Analytical sensitivity derivatives facilitate an efficient optimization process that allows a relatively large number of design variables. Standard finite element and unsteady aerodynamic routines are used to construct a modal data base. Minimum-state aerodynamic approximations and dynamic residualization methods are used to construct a high-accuracy, low-order aeroservoelastic model. Sensitivity derivatives of flutter dynamic pressure, control stability margins, and control effectiveness with respect to structural and control design variables are presented. A gradient-based constrained optimization algorithm is used to minimize an overall cost function. A realistic numerical example of a composite wing with four controls is used to demonstrate the modeling technique, the optimization process, and their accuracy and efficiency.

Nomenclature

$[\hat{A}]$ = closed-loop system matrix
$[\bar{A}]$ = closed-loop system matrix after truncation
$[\bar{\bar{A}}]$ = closed-loop system matrix after residualization
$[A]$, $[B]$, $[C]$, $[D]$ = state-space coefficient matrices, Eq. (11)
A_f, A_g, A_W = cost function weighting parameters
$[B_s]$ = generalized damping matrix
b = semicord
C_i, C_{0_i} = equality constraint coefficients, Eq. (22)
$[\bar{F}]$, $[\bar{G}]$, $[\bar{H}]$ = residualization constraint matrices, Eq. (15)
G = control gain
G^* = control gain at which instability occurs
$\bar{G}$ = upper limit of G
$[G]$ = control gain matrix
GM = control gain margin
GM_0 = requested minimal gain margins
$[I]$ = identity matrix
J = optimization cost function, Eq. (26)
$[K_i]$, $[M_i]$ = contributions of a unit structural design variable to the mass and stiffness matrices
$[K_s]$ = generalized stiffness matrix
$[\bar{K}_s]$ = generalized stiffness matrix of elastic modes
k = reduced frequency, $\omega b/V$
k_i = tabulated reduced frequency
$\bar{L}$, $\bar{L}$ = available and required control rolling moments per unit aircraft roll rate
$\bar{L}_\delta$ = rigid aerodynamic rolling moment per unit dynamic pressure due to unit control surface deflection
$[M]$ = mass matrix
$[M_c]$ = generalized control coupling mass matrix
$[M_f]$ = fictitious mass matrix
$[M_s]$ = generalized mass matrix
n = number of states
n_s = number of retained elastic modes
p = design variable
p_s = structural design variable
$\bar{p}_s$ = upper limit of p_s
$[Q_c]$, $[Q_s]$ = control and structural columns of the generalized unsteady aerodynamic force coefficient matrix
$[Q_c^*]$, $[Q_s^*]$ = weighted aerodynamic matrices
$[\bar{Q}_c]$, $[\bar{Q}_s]$ = portions of $[Q_c(0)]$ and $[Q_s(0)]$, Eq. (17)
Q_1^*, Q_2^* = measures of aeroservoelastic importance, Eqs. (13) and (14)
q = dynamic pressure
q_d = design dynamic pressure
q_f = flutter dynamic pressure
q_{f_0} = requested minimal flutter dynamic pressure
s = Laplace variable
$\bar{s}$ = nondimensionalized Laplace variable, sb/V
T = transfer function from sensor to control surface
$\{U\}$, $\{V\}$ = column and row eigenvectors for $[\bar{A}]$
$\{u\}$ = actuator command input vector
V = flow velocity
w_i = added weight due to unit p_i
$\{x\}$ = state vector
$\{x_a\}$ = aerodynamic augmenting states
$\{x_c\}$ = control system states
$\{x_e\}$, $\{x_c\}$ = eliminated and retained states
$\{y\}$ = sensor output vector
$[\Delta\bar{K}_s]$ = addition to generalized stiffness matrix; Eq. (19)
ΔW, ΔW_0 = added weight and its requested upper limit
$\{\delta\}$ = control surface deflection vector
ζ = equivalent viscous modal damping coefficient
η = aeroelastic effectiveness
λ = eigenvalue of $[\bar{A}]$
λ_f = flutter eigenvalue
$\{\xi\}$ = generalized structural displacement vector
$\{\xi_e\}$, $\{\xi_r\}$ = eliminated and retained structural displacements
$[\psi_c]$ = control surface deflection modes
$[\psi_m]$ = vibration mode shapes of the baseline structure
$[\bar{\psi}_m]$ = approximated mode shapes of the baseline structure

Received Jan. 7, 1991; revision received June 20, 1991; accepted for publication Sept. 9, 1991.

*Associate Professor, Faculty of Aerospace Engineering. Member AIAA.

$[\psi_{mf}]$ = fictitious control surface deflections in structural modes
$[\psi_s]$ = sensor input modal slopes
ω = vibration frequency
ω_f = flutter frequency
ω_n = natural frequency
$\partial/\partial\bar{p}$, $\partial/\partial\tilde{G}$ = constrained derivatives, Eqs. (23) and (24)

Introduction

THE design of the structural and control systems of a flight vehicle with a given aerodynamic configuration starts with separate analyses which are aimed at satisfying basic stress and performance requirements. These preliminary designs are then optimized to satisfy structural and control stability margin requirements with a minimal performance cost and without violating the design constraints. Modern high-performance, control-augmented aircraft may have a strong coupling between the structural and control systems through aeroelastic effects. This calls for a multidisciplinary optimization process in which structural and control design variables are modified simultaneously.

The purpose of this work is to present a practical and efficient optimization scheme in which the various aeroservoelastic aspects are analyzed and synthesized with a common model. The applicability of the common-model approach to realistic design cases has been demonstrated by Livne et al.[1,2] who presented an integrated synthesis scheme that can treat a rich variety of behavior constraints and performance measures such as stress, displacements, control surface travel and hinge moments, aeroservoelastic poles, gust response, drag, and aircraft maneuver parameters. A thorough literature survey is also given in Ref. 1. The structural model of Refs. 1 and 2 is based on the equivalent plate approach of Giles[3] with which a complex structure can be represented by a relatively low number of degrees of freedom. This allows the inclusion of the entire structural model in the aeroservoelastic model, which is impractical with common finite element models like those of NASTRAN.

The optimization model suggested in this paper is based on data that can be extracted from any linear structural, aerodynamic, and control models. It is assumed that the structure can be represented in the optimization by a limited set of low-frequency vibration modes of the baseline finite element model. The validity and limitations of this assumption in practical applications are examined in this work by numerical examples. The general scheme of a major optimization cycle is given in Fig. 1. An aeroelastic modal data base is first constructed for a relatively large number of modes. The computational efficiency of this part is not as important as that of the later parts because it is performed once for the entire optimization process or at least for the major part of it. The aeroservoelastic modeling part of the scheme is aimed at resulting in a model of minimal size but still accurate enough for the optimization process. Several size-reduction techniques are combined to achieve this goal and to provide the analyst with physical insight and numerical measures for an a priori evaluation of the size-reduction effects. The third part of the optimization scheme is the actual model update process to minimize a cost function within the design constraints. High computational efficiency of this part facilitates an interactive design process where the designer can inspect the results and change parameters in order to perform tradeoff studies and to obtain a realizable design.

The design objectives in this work are to satisfy given requirements for flutter and control stability margins and to achieve the desired roll performance with a minimal weight penalty and without exceeding the limits of the design variables. For the sake of clarity we start with the description of the test-case model that will be used to demonstrate the various parts of the optimization process. The formulation and applications elaborate on the new features of this work in the area of reduced-size modeling, sensitivity derivatives of stability margins and aeroelastic effectiveness, and the model update process.

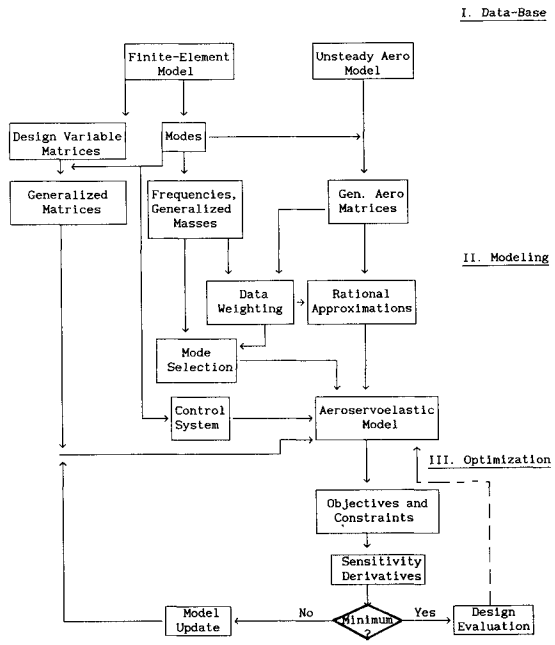

Fig. 1 General scheme of a major optimization cycle.

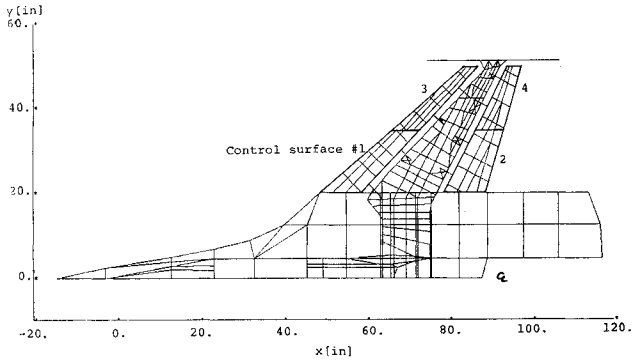

Fig. 2 Top view of the AFW structural model.

Table 1 Natural frequencies and modes of the baseline structure

Mode no.	Frequency, Hz	Description
1	0.	Rigid body roll
2	7.023	1st fuselage bending
3	7.856	1st wing bending
4	13.069	Missile pitch
5	16.161	2nd fuselage bending
6	27.408	2nd wing bending
7	38.271	1st wing torsion
8	39.639	Missile yaw
9	41.137	Fuselage torsion
10	49.922	3rd fuselage bending
11	51.640	3rd wing bending
12	57.403	2nd wing torsion

Test-Case Model

The test-case deals with the active-flexible-wing (AFW) composite wind-tunnel model tested at NASA Langley Research Center. A top view of the NASTRAN finite element model is given in Fig. 2. A description of the aerodynamic model appears in Ref. 4. The mathematical model assumes antisymmetric boundary conditions at Mach 0.9. The lowest 12 vibration frequencies and the associated mode descriptions appear in Table 1.

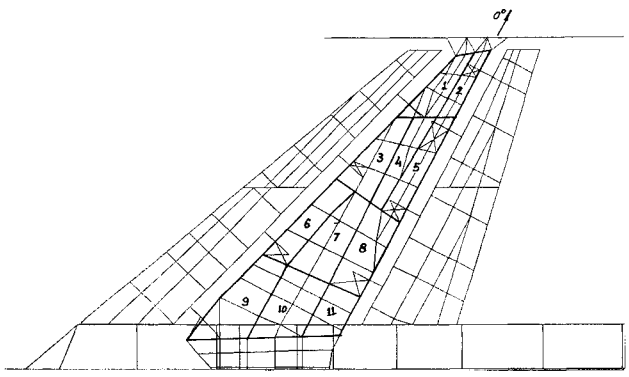

Fig. 3 Wing-box optimization zones.

The subject for optimization is the wing-box structure between $y = 18.45$ in. and $y = 49.30$ in. The wing-box composite upper and lower skins are mirror images of each other. The wing-box is divided into 11 optimization zones as shown in Fig. 3. The baseline weight of the optimized portion of the structure is 3.06 lb. The total number of high-strength graphite-epoxy plies in each of the skins varies between four at zone 2 (one in each of the 0-, +45-, −45-, and 90-deg orientations) and 20 at zone 9 (four in 0-deg and two in each of the 28-, −62-, 45-, −45-, 73-, −17-, and 90-deg orientations).

The model has four control surfaces per wing (see Fig. 2) driven by third-order actuators. A zero-order control system reads the output of a roll rate-gyro located near the centerline and commands the actuators through different gains. A performance analysis established that a control law which supplies a rolling moment of $L \leq \bar{L}$, where $\bar{L} = 3000$ lb-in. per unit aircraft roll rate (minus pilot roll command), is required for adequate roll performance at the design dynamic pressure $q_d = 1.5$ psi. L is related to the control, aerodynamic, and aeroelastic parameters by

$$\Sigma G_i \eta_i \bar{L}_{\delta_i} = L/q_d \tag{1}$$

where $\bar{L}_{\delta_i}$ is the rigid aerodynamic rolling moment per unit dynamic pressure due to unit deflection of the ith control surface and G_i and η_i are the associated control gain and aeroelastic effectiveness. In addition, the closed-loop aeroservoelastic system is required to exhibit a sufficient flutter margin:

$$q_f \geq 1.44 q_d \tag{2}$$

All the nonzero gains are required to exhibit sufficient gain margins

$$|GM_i| \geq 6db \tag{3}$$

where $GM_i = 20 \log(G_i^*/G_i)$ where G_i^*/G_i is a positive factor by which G_i has to be multipled to achieve instability at q_d (with other gains remaining unchanged). $G_i^*/G_i > 1$ yields the positive gain margin, and $G_i^*/G_i < 1$ yields the negative one. Phase margin requirements and their sensitivity derivatives are given in Ref. 5. They are not discussed here because they are not critical in the test-case problem of this paper.

Aeroelastic Data Base

The aeroelastic data base (see top part of Fig. 1) has been constructed using the MSC/NASTRAN code. The modes consist of the 25 lowest frequency vibration modes of the baseline structure $[\psi_m]$ and four control surface deflection modes $[\psi_c]$ of unit rotation of the respective control surface and zero deflection elsewhere. The modes serve as generalized coordinates in the Laplace domain equation of motion

$$[C_s(s)]\{\xi(s)\} = -([M_c]s^2 + q[Q_c(s)])\{\delta(s)\} \tag{4}$$

where

$$[C_s(s)] = ([M_s]s^2 + [B_s]s + [K_s] + q[Q_s(s)])$$

where $[M_s]$, $[B_s]$ and $[K_s]$ are the generalized structural mass, damping, and stiffness matrices respectively, $[M_c]$ is the control coupling mass matrix, $\{\xi\}$ is the vector of generalized structural displacements, $\{\delta\}$ is the vector of control surface commanded deflections, $[Q_s(s)]$ and $[Q_c(s)]$ are the generalized unsteady aerodynamic force coefficient matrices, and q is the dynamic pressure. For the baseline structure $[M_s]$ and $[K_s]$ are diagonal. $[B_s]$ is also assumed to be diagonal with $B_{s_i} = 2\zeta_i M_{s_i} \omega_{n_i}$ where ζ_i is the equivalent viscous modal damping coefficient and ω_{n_i} is the ith natural frequency. $[M_c]$ is defined by

$$[M_c] = [\psi_m]^T [M][\psi_c] \tag{5}$$

where $[M]$ is the mass matrix in discrete coordinates. The computation of the baseline coefficient matrices of Eq. (4) starts with normal modes analysis of the free undamped structure. A convenient way to have $[\psi_m]$ and $[\psi_c]$ included in a unified set of modes, such that the matrices on the right-hand side of Eq. (4) can be calculated along with those on the left-hand side, is as following. The finite element model is changed such that each control surface is disconnected from its actuator. The differential motion between the two sides of each disconnection point defines a new DOF, δ_i, which represents the rigid-body rotation of the ith control surface relative to the wing. Each δ_i is loaded with a fictitious mass M_{f_i} of large magnitude. A thorough discussion on the use of fictitious masses in normal modes analysis is given in Ref. 6. The resulting modes include $[\psi_c]$ as rigid-body modes while the other modes, frequencies, and generalized masses are approximately equal to those of the original structure. Each control surface mode is normalized to a unit deflection of the respective δ_i. Orthogonality between the rigid-body control surface modes and the others implies

$$\begin{bmatrix} \bar{\psi}_m \\ \bar{\psi}_{mf} \end{bmatrix}^T \begin{bmatrix} M & 0 \\ 0 & M_f \end{bmatrix} \begin{bmatrix} \psi_c \\ I \end{bmatrix} = [0] \tag{6}$$

where the matrices are partitioned according to the original coordinates and the added ones. It can be shown that $[\bar{\psi}_m]$ becomes closer to $[\psi_m]$ with increasing magnitudes of $[M_f]$ which yields via Eqs. (5) and (6)

$$[M_c] = -[\psi_{mf}]^T [M_f] \tag{7}$$

which is used in lieu of Eq. (5). The test-case analysis was performed with the 4×4 $[M_f]$ matrix equal $[I]10^6$ while the maximum value of the other terms in the mass matrix is less than 1. Comparison of frequencies and modes of the original model with those of the fictitious-masses one showed that they were practically identical. Consequently, the entire data base was constructed with the modified model. $[B_s]$ was constructed with all $\zeta_i = 0.01$.

The unsteady aerodynamic code is employed to calculate $[Q_s]$ and $[Q_c]$ of Eq. (4) (using $[\bar{\psi}_m]$ and $[\psi_c]$) for various values of the nondimensionalized Laplace variable $\bar{s} = ik$ where k is the reduced frequency $\omega b/V$ where ω is the vibration frequency, b is a reference semichord, and V is the flow velocity. The aerodynamic database of the test-case includes 13 generalized aerodynamic matrices for the k values of 0., 0.05, 0.1, 0.2, 0.3, 0.4, 0.5, 0.7, 1.0, 1.4, 1.9, 2.5, and 3.1.

The remaining part of the aeroelastic data base is the data needed for the structural optimization. A structural design variable (p_{s_i}) in our case is the thickness of a composite fiber ply added to the upper and lower surfaces of one of the zones of Fig. 3. The added ply thicknesses are treated in this work as continuous parameters where a unit value represents the

thickness of a single ply. Three design variables, representing the 0-, 45-, and −45-deg orientations are assigned for each zone. The incremental stiffness and mass contributions, $[K_i]$ and $[M_i]$, of a unit p_{s_i} to the full-size stiffness and mass matrices are calculated by the finite-element code and pre and post multiplied by the appropriate partitions of $[\psi_m]$ to yield

$$\frac{\partial[K_s]}{\partial p_{s_i}} = [\psi_m]^T[K_i][\psi_m] \tag{8a}$$

$$\frac{\partial[M_s]}{\partial p_{s_i}} = [\psi_m]^T[M_i][\psi_m] \tag{8b}$$

which are valid as long as we keep $[\psi_m]$ unchanged. It is assumed that $\partial[B_s]/\partial p_{s_i} = 0$. Expressions for the derivative of $[M_c]$ with respect to p_{s_i} are given in Ref. 5. In our case $\partial[M_c]/\partial p_{s_i} = 0$ because the masses of the control surfaces are not modified throughout the optimization. The geometrical changes due to adding plies to the wing surface (stacking effects) are assumed in this work to be negligible.

The derivative matrices of Eqs. (8a) and (8b) with respect to all the structural design variables are stored in the data base. A major feature of the presented optimization scheme is based on the assumption that the displacements of the modified structure may be described as a linear combination of the baseline modes $[\psi_m]$ which serve as unchanged generalized coordinates throughout the process. The nondiagonal derivative matrices are multiplied after each step by the current values of p_{s_i} and then added to the diagonal baseline generalized stiffness and mass matrices. Even though the generalized coordinates do not change, the coupling terms cause the natural vibration modes to change in a way that removes the mode coupling that causes flutter.

Aeroservoelastic Modeling and Stability Analysis

The aeroservoelastic modeling process (see part II of Fig. 1) is aimed at obtaining an efficient constant coefficient, state-space model to be used in the simultaneous structural and control optimization. The state-space formulation requires the tabulated $[Q_s(ik_\iota)]$ and $[Q_c(ik_\iota)]$ matrices to be approximated by rational functions. A review and extensions to the most common rational approximation methods and the associated model formulations are given in Ref. 7. Among those, the Minimum-State (MS) method[8,9] has been shown in several applications to realistic problems[9,10,11] to yield the most efficient aeroservoelastic models per desired accuracy. Best MS results are obtained when the physical weighting algorithm of Ref. 9, which weights the tabulated aerodynamic terms according to their aeroservoelastic importance, is applied. A $Q_{s_{ij}}$ term of $[Q_s(ik_\iota)]$ is weighted according to its contribution to the response of ξ_j of the open-loop baseline system of Eq. (4) with $q = q_d$ and $s = ik_\iota V/b$ to sinusoidal excitation by the jth column of $[Q_s(ik_\iota)]$. The resulting weighted aerodynamic terms are

$$Q^*_{s_{ij}}(ik_\iota) = |\bar{C}_{s_{ji}}(ik_\iota)|Q_{s_{ij}}(ik_\iota) \tag{9}$$

where $\bar{C}_{s_{ji}}(ik_\iota)$ is the jith term of $[C_s(ik_\iota)]^{-1}$ of Eq. (4). A $Q_{c_{ij}}$ term of $[Q_c(ik_\iota)]$ is weighted according to its contribution to the open-loop response of the jth actuator output to sinusoidal excitation by the jth column of $[Q_c(ik_\iota)]$. The resulting weighted aerodynamic terms are

$$Q^*_{c_{ij}}(ik_\iota) = |\bar{C}_{c_{ij}}(ik_\iota)|Q_{c_{ij}}(ik_\iota) \tag{10}$$

where

$$\bar{C}_{c_{ij}}(ik_\iota) = i\frac{k_\iota V}{b}T_j(ik_\iota)[\psi_s]\{\bar{C}_s(ik_\iota)\}_i$$

where T_j is the nominal control system transfer function from sensor output to the jth actuator output, $[\psi_s]$ is a row vector of modal slopes at the sensor input and $\{\bar{C}_s\}_i$ is the ith column of $[C_s(ik_\iota)]^{-1}$. The weighted terms of Eqs. (9) and (10) are normalized such that the maximum magnitude in each group is 1.0. As depicted in Refs. 9 and 12, the weighted magnitudes may exhibit sharp peaks when plotted vs k_ι. In order to extend the validity of the aerodynamic approximation to a wide range of parametric changes and to avoid approximation least-square problems, the peaks are widened by 2 widening cycles as described in Ref. 12. The aerodynamic matrices associated with the 25 vibration modes and the 4 control modes were approximated with 6 MS approximation roots, which yield only 6 aerodynamic augmenting states.

The formulation of the resulting aeroservoelastic model is presented in Refs. 5 and 9. The open-loop state-space equations are in the form of

$$\{\dot{x}\} = [A]\{x\} + [B]\{u\} \tag{11a}$$

$$\{y\} = [C]\{x\} + [D]\{u\} \tag{11b}$$

where $\{x\}$ is the state vector combined of the structural states $\{\xi\}$ and $\{\dot{\xi}\}$, the aerodynamic augmenting states $\{x_a\}$ and the control system states $\{x_c\}$, $\{u\}$ is the actuator command inputs, and $\{y\}$ is the sensor output vector. The control loop can be closed via a gain matrix $[G]$ that relates $\{u\}$ to $\{y\}$, which results in the closed-loop equation

$$\{\dot{x}\} = [\hat{A}]\{x\} \tag{12}$$

where

$$[\hat{A}] = [A] + [B]([I] - [G][D])^{-1}[G][C]$$

In our case, the full-size model has $n = 68$ states (50 structural, 6 aerodynamic, and 12 control states). The eigenvalues of the constant coefficient, real-valued matrix $[\hat{A}(q)]$ are used to analyze the system stability. Root locus analysis with variable q yields the flutter dynamic pressure, q_f, at which one of the root branches crosses to the right-hand side of the Laplace domain. The gain margins defined after Eq. (3) are found by a root locus analysis at $q = q_d$ with variable G_i which yields the instability gain G_i^*. More details and numerical examples for the calculation of flutter, gain, and phase margins are given in Ref. 5. The accuracy of the MS approximation in the test-case has been examined by comparing flutter results with those of MSC/NASTRAN (using the PK method). The differences in q_f and ω_f were less than 1%.

Model Size Reduction

The computational efficiency of the optimization process is approximately proportional to n^3. It is therefore desired to reduce n as much as accuracy allows. The vibration modes are divided for this purpose into three groups, those which may be truncated, those which may be eliminated via residualization, and those which remain in the model as independent states. The physical weighting of Eqs. (9) and (10) has been found to be a helpful guide in the mode selection process. Two measures of aeroservoelastic importance are assigned to each mode. The measures are

$$Q^*_{1_i} = \max_{j,\,\iota}\{|Q^*_{s_{ij}}(ik_\iota)|\} \tag{13}$$

and

$$Q^*_{2_i} = \max_{j,\,\iota}\{|Q^*_{c_{ij}}(ik_\iota)|\} \tag{14}$$

The modal measures of aeroservoelastic importance of 17 of the 25 data base modes are given in Table 2 in decreasing order of overall importance. The other 8 modes (numbers 10, 14, 15, 17, 19, 20, 21, and 23), for which both $Q^*_{1_i}$ and $Q^*_{2_i}$ are less than 0.01, are truncated. The 6 modes in the second

Table 2 Modal measures of aeroservoelastic importance

Mode no.[a]	Q_1^*	Q_2^*
1	0.482	1.000
4	1.000	0.125
3	0.611	0.404
6	0.512	0.035
12	0.264	0.034
2	0.149	0.114
11	0.161	0.035
7	0.175	0.023
9	0.135	0.026
5	0.022	0.035
8	0.031	0.009
16	0.033	0.003
18	0.024	0.007
24	0.023	0.005
25	0.024	0.003
22	0.019	0.004
13	0.017	0.004

[a]The other modes have Q_1^* values of less than 0.01.

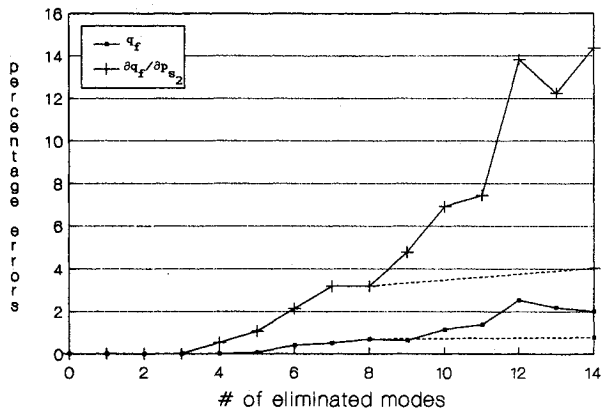

Fig. 4 Size-reduction effects on flutter dynamic pressure and its sensitivity derivatives.

group of Table 2 are eliminated via residualization, and the 11 modes in the first group of Table 2 are retained as independent variables.

The truncation is performed by crossing-out the associated rows and columns in $[\hat{A}]$ of Eq. (12). The resulting closed-loop system matrix $[\bar{A}]$ forms the basis for subsequent residualization.

The formulations of model size reduction via static and dynamic residualization are given in Ref. 4. The most general constraints that allow model size reduction for stability analysis are

$$\{x_e\} = [\bar{F}]\{x_r\} + [\bar{G}]\{u\} + [\bar{H}]\{\dot{x}_r\} \tag{15}$$

where $\{x_e\}$ is the vector of eliminated structural states $\{\xi_e\}$ and $\{\dot{\xi}_e\}$ and $\{x_r\}$ is the vector of the retained states $\{\xi_r\}$, $\{\dot{\xi}_r\}$, $\{x_a\}$, and $\{x_c\}$. The coefficient matrices of Eq. (15) are derived in Ref. 4 using Eq. (11) and neglecting some terms associated with the eliminated states. In static residualization, the rows of $[\bar{F}]$ and $[\bar{H}]$ which are associated with $\{\dot{\xi}_e\}$, and the entire $[\bar{G}]$ are zero, which has a computational advantage in the residualization process. However, the dynamic residualization, which is used in this work, typically yields a better overall efficiency because it allows the elimination of more modes per desired accuracy.[4] Equations (11), (12), and (15) are combined in Ref. 4 to yield the residualized closed-loop equation

$$\{\dot{x}_r\} = [\bar{A}]\{x_r\} \tag{16}$$

which is used in this work in lieu of Eq. (12) in the root-locus analysis described in the previous section.

The effects of truncation and residualization on q_f and on its derivative with respect to p_{s_2} (which is described in the sensitivity derivative section below) are shown in Fig. 4. The solid lines give the percentage errors introduced by truncation vs the number of truncated modes. The baseline values of $q_f = 1.736$ psi and $\partial q_f/\partial p_{s_2} = 0.188$ psi have been obtained with the full 25 mode model where the gain values associated with the four control surfaces are 0.0, −0.1, −0.1 and 0.0664, respectively. The modes truncated at each point of Fig. 4 are those with the lowest measures of aeroservoelastic importance defined by Eqs. (13) and (14). It can be deduced from the error rates of change that the usage of these measures for mode selection is adequate. The errors due to the truncation of 8 modes plus residualization of 6 modes, given at the ends of the dashed lines, demonstrate the accuracy of the dynamic residualization relative to that of truncation.

Control Effectiveness

The control effectiveness parameters in Eq. (1) and their sensitivity derivatives are needed to be calculated repeatedly throughout the optimization process. Application of the discrete approach of Ref. 13 would impose a severe computational cost. The 25-mode data base described above facilitated an efficient utilization of the modal approach of Ref. 14. The real-valued $[Q_s(0)]$, $[Q_c(0)]$ and $[K_s]$ of Eq. (4) are partitioned into the rigid and elastic mode partitions

$$[Q_s(0)] = \begin{bmatrix} \bar{Q}_{s11} & \bar{Q}_{s12} \\ \bar{Q}_{s21} & \bar{Q}_{s22} \end{bmatrix}; \qquad [Q_c(0)] = \begin{bmatrix} \bar{Q}_{c1} \\ \bar{Q}_{c2} \end{bmatrix} \tag{17}$$

and

$$[K_s] = \begin{bmatrix} 0 & 0 \\ 0 & \bar{K}_s \end{bmatrix}$$

When there is a single rigid body mode in roll, the effectiveness of rolling moment due to unit deflection of the ith control surface is

$$\eta_j = 1 - \frac{q_d}{\bar{Q}_{c_{1_j}}} [\bar{Q}_s]_{12}[\bar{K}]^{-1}\{\bar{Q}_c\}_{2_j} \tag{18}$$

where $\{\bar{Q}_c\}_{2_j}$ is the jth column of $[\bar{Q}_c]_2$ and

$$[\bar{K}] = [\bar{K}_s] + [\Delta\bar{K}_s] + q_d[\bar{Q}_s]_{22} \tag{19}$$

where

$$[\Delta\bar{K}_s] = \sum_i \frac{\partial[\bar{K}_s]}{\partial p_{s_i}} p_{s_i}$$

where $\partial[\bar{K}_s]/\partial p_{s_i}$ is calculated by Eq. (8a) using elastic modes only. The differential of Eq. (18) with respect to a structural design variable p_{s_i} yields

$$\frac{\partial \eta_i}{\partial p_{s_i}} = \frac{q_d}{\bar{Q}_{c_{1_j}}} [\bar{Q}_s]_{12}[\bar{K}]^{-1} \frac{\partial[\bar{K}_s]}{\partial p_{s_i}} [\bar{K}]^{-1}\{\bar{Q}_c\}_{2_j} \tag{20}$$

It should be noted that the calculation of all the control effectiveness parameters in Eq. (18) and all their derivatives in Eq. (20), for a given set of design variables, involves only one matrix inversion of order n_s where n_s is the number of elastic modes after truncation (16 in our case).

The variation of η_4 and $\partial\eta_4/\partial p_{s_2}$, divided by their baseline values, with the number of low frequency modes taken into account are shown in Fig. 5. The baseline values, calculated by all the data base modes are $\eta_4 = 0.216$ and $\partial\eta_4/\partial p_{s_2} = 0.0079$. The stars indicate the modes which will be actually truncated in the optimization. The convergence rates demonstrate the adequacy of the modal approach in considering control effectiveness in structural optimization. It should be

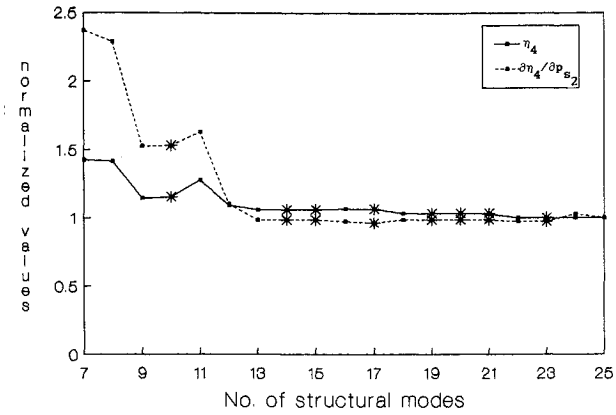

Fig. 5 Control effectiveness variations with number of structural modes taken into account.

noticed, however, that the convergence of the sensitivity derivatives is slower than that of η itself.

Stability and Sensitivity Derivatives

Expressions for sensitivity derivatives of the flutter dynamic pressure q_f and gain margins GM_i with respect to structural and control design variables are developed in Ref. 5. They are based on the neutral stability eigenvalues, the associated column and row eigenvectors and the derivatives of $[\bar{A}]$, namely the truncated system matrix before residualization. The derivative of an eigenvalue λ with respect to a design variable p_j is

$$\frac{\partial\lambda}{\partial p_j} = \frac{\{V\}^T \frac{\partial[\bar{A}]}{\partial p_j}\{U\}}{\{V\}^T\{U\}} \tag{21}$$

where $\{V\}$ and $\{U\}$ are the row and column eigenvectors of $[\bar{A}]$ associated with λ. The neutral stability eigenvalue $\lambda_f = i\omega_f$ associated with either q_f or GM_i is found by root locus analysis of the residualized system matrix $[\bar{A}]$ of Eq. (16). It is assumed that λ_f is also an eigenvalue of $[\bar{A}]$. The derivatives of $[\bar{A}]$ with respect to the structural design variables[5] are based on the data base stiffness and mass derivatives of Eq. (8).

The neutral stability parameters and their derivatives calculated in an optimization step are used to calculate a first-order guess of the next step neutral stability parameters such that the number of eigen solutions in the next step root locus analysis is minimal.

Optimization Constraints

The optimization process is subject to sets of equality and inequality constraints which are defined by the analyst to achieve a realizable design which satisfies the requirements.

Equality constraints are defined in the form

$$\sum C_i p_i = C_0 \tag{22}$$

where the C_i values may be functions of other design variables. For each constraint equation one of the independent design variables, p_k which has non-zero C_k, is defined as a dependent variable. The differential of Eq. (22) with respect to an independent design variable, p_j, yields the constrained derivatives

$$\frac{\partial}{\partial\tilde{p}_j} = \frac{\partial}{\partial p_j} - \frac{1}{C_k}\left(C_j + \sum_i \frac{\partial C_i}{\partial p_j} p_i\right)\frac{\partial}{\partial p_k} \tag{23}$$

The inequality constraints are divided into two groups. In the first group are those whose boundaries can be defined in the form of Eq. (22). This group includes limits on the structural gauges and control gains, and the rolling moment requirement of Eq. (1). Other inequality requirements, like the q_f and GM_i requirements of Eqs. (2) and (3) are assigned a penalty function and included in the optimization cost function discussed in the following section.

The baseline model satisfies all the inequality constraints of the first group. One of the design variables p_ι in each inequality constraint is defined as a compensating variable. If the boundary equation is satisfied at the beginning of an optimization step, and the steepest descent vector is into the unfeasible domain, the inequality constraint becomes active, p_ι becomes a dependent variable and the cost function sensitivity derivatives are modified using Eq. (23). At the end of the optimization step, the p_ι values of the active constraints, and those of the inactive ones which are violated by this step, are calculated using Eq. (22).

In our test-cases, the rolling moment requirement of Eq. (1) was active throughout the optimizations. The control gain G_4 is defined as a dependent variable, which yields, via Eq. (23), the constrained derivatives with respect to other gains

$$\frac{\partial}{\partial\tilde{G}_j} = \frac{\partial}{\partial G_j} - \frac{\eta_j\bar{L}_{\delta_i}}{\eta_4\bar{L}_{\delta_4}}\frac{\partial}{\partial G_4} \tag{24}$$

and the constrained derivatives with respect to the structural design variables

$$\frac{\partial}{\partial\tilde{p}_{s_j}} = \frac{\partial}{\partial p_{s_j}} - \frac{1}{\eta_4\bar{L}_{\delta_4}}\left(\sum_i \frac{\partial\eta_i}{\partial p_{s_j}}\bar{L}_{\delta_i}G_i\right)\frac{\partial}{\partial G_4} \tag{25}$$

The inequality constraints associated with structural gauge and control gain limits are considered prior to the rolling moment requirement such that Eqs. (1), (24), and (25) are applied with feasible values. It can be shown that the suggested constraint procedure leads to a design that satisfies the Kuhn-Tucker optimality criteria of Ref. 15.

Optimization Process

Three cases of the baseline structure with different control gains are given in Table 3. All the cases are with $G_1 = 0.0$ and satisfy the rolling requirement of Eq. (1) with $L = \bar{L}$. Case 1 is with $G_2 = G_4$ and $G_3 = 0$, which yields $q_f < q_d$. Since $\partial q_f/\partial G_4$ is relatively large and η_4 is relatively small, G_4 can be reversed to suppress flutter while G_2 and G_3 compensate for the loss of rolling moment. This is utilized in cases 2 and 3 in which $q_f > q_d$, but the flutter and gain margin requirements of Eqs. (2) and (3) are not met. Even though the main participants in the flutter mechanisms of cases 2 and 3 are the same modes (3 and 4 of Table 1), the flutter frequency, gain margins, and the derivatives are substantially different, which indicates a high sensitivity of the stability characteristics to parametric changes.

To obtain a balanced structural design, all the design variables associated with the −45-deg ply direction are constrained to be equal to the +45-deg ones. It is assumed that the structure is already sized for stress. To avoid violation of

Table 3 Three baseline design cases with different control gains

Parameter	Case 1	Case 2	Case 3
G_2	−0.0871	−0.09	−0.1
G_3	0.0	−0.09	−0.1
G_4	−0.0871	0.0203	0.0667
q_f, psi	0.633	1.564	1.745
ω_f, rad/sec	78.910	74.646	55.180
GM_2, db	—	0.798	7.993
GM_3, db	—	0.613	8.743
GM_4, db	—	9.231	4.148
$\partial q_f/\partial G_2$	1.94	6.97	−1.62
$\partial q_f/\partial G_3$	2.81	9.30	1.27
$\partial q_f/\partial G_4$	5.00	45.04	−10.02
$\partial q_f/\partial\tilde{G}_2$	−3.82	−153.4	34.06
$\partial q_f/\partial\tilde{G}_3$	−15.86	−39.3	12.09

stress requirements and to obtain a smooth design, all the structural variables are limited to $0 \le p_{si} \le \bar{p}_s$ where $\bar{p}_s = 1.0$ in zones 1 and 2 of Fig. 3, 2.0 in zones 3 to 5, 3.0 in zones 6 to 8, and 4.0 in zones 9 to 11. The control gains are constrained to $G_1 = 0$ and the others to $|G_i| \le \bar{G}$ where $\bar{G}$ is equal to either 0.09 or 0.1. The independent design variables before activating inequality constraints are the 22 0-deg and 45-deg structural variables and the three control gains (G_2, G_3, and G_4).

A preliminary analysis indicated that the critical stability parameters are q_f and the positive gain margins. Consequently, the cost function to be minimized is

$$J = e^{A_W(\Delta W - \Delta W_0)} + e^{A_f(q_{f0} - q_f)} + \sum_{j=2}^{4} e^{A_{gj}(GM_0 - GM_j)} \quad (26)$$

where q_{f0} and GM_0 are the requested flutter dynamic pressure and gain margins, ΔW is the added weight, ΔW_0 is the allowed weight penalty and A_W, A_f, and A_{gj} are cost-weighting parameters. The sensitivity derivatives of J are

$$\frac{\partial J}{\partial p_i} = A_W w_i e^{A_W(\Delta W - \Delta W_0)} - A_f \frac{\partial q_f}{\partial p_i} e^{A_f(q_{f0} - q_f)} - \sum_{j=2}^{4} A_{gj} \frac{\partial GM_j}{\partial p_i} e^{A_{gj}(GM_0 - GM_j)} \quad (27)$$

where p_i is either a structural variable p_{si} or a gain G_i and w_i is $\partial W/\partial p_i$.

A steepest descent optimization algorithm has been used to perform the four optimization cases presented in Tables 4 and 5. Case I of Table 4 has been performed to find the optimal gains, limited by $\bar{G} = 0.1$, without changing the structure. The results are close to those of case 3 of Table 3, but with better q_f and gain margins. However, q_f does not satisfy the required margins. The simultaneous structure and gain optimization of case II yields sufficient margins at the penalty of adding 0.07 lb to the structure. It can be noticed from case II of Table 5 that the 0-deg plies in the wing root zones 9 and 10 and in the wing tip zones 1 and 2 are the most effective. The 45-deg plies of zones 3 and 4 have also some effect, while the others are either not effective or constrained to the minimum gauge. Case III is the same as II, but with $G_3 = 0$. The required margins are also met, but with a weight penalty of 0.277 lb, which is about 9% of the optimized portion of the structure. The flutter frequency and the structural changes are substantially different than those of case II. The 0-deg and 45-deg plies of zones 1 and 2, and the 45-deg plies of zones 3 to 5 achieve their maximum limits while all the others remain at or close to the minimum limits. Case IV is the same as case II, but with gain limits of $\bar{G} = 0.9$. The optimization process stopped in this case when the number of active constraints reached the number of design variables. The differences between the resulting structures of Table 5 demonstrate the importance of simultaneous structural and control optimization of aeroservoelastic systems.

Table 4 Four optimization cases

Parameter	Case I gain only	Case II	Case III $G_3 = 0$	Case IV
$\bar{G}$	0.1	0.1	0.1	0.09
ΔW, lb	0.	0.070	0.277	0.287
q_f, psi	2.031	2.191	2.183	2.620
ω_f, rad/s	51.397	59.307	83.610	66.420
GM_2, db	6.57	6.56	9.57	6.39
GM_3, db	7.48	6.69	—	5.24
GM_4, db	7.07	8.37	8.92	8.84
G_2	−0.0974	−0.0974	−0.1	−0.09
G_3	−0.0914	−0.0901	0.0	−0.09
G_4	0.0481	0.0435	−0.0315	0.0230

Table 5 Structural changes (p_{si}) in cases II to IV

i	Zone	Ply direction, deg	Case II	Case III	Case IV
1	1	0	0.199	1.	0.
2	1	45	0.020	1.	0.
3	2	0	0.317	1.	0.
4	2	45	0.015	1.	0.
5	3	0	0.002	0.	0.
6	3	45	0.098	2.	0.
7	4	0	0.	0.	0.
8	4	45	0.157	2.	0.
9	5	0	0.014	0.	0.
10	5	45	0.035	2.	0.
11	6	0	0.	0.	0.
12	6	45	0.075	0.	0.
13	7	0	0.	0.	0.
14	7	45	0.	0.	0.
15	8	0	0.	0.	0.
16	8	45	0.	0.	0.
17	9	0	0.538	0.	4.
18	9	45	0.	0.	0.
19	10	0	1.346	0.092	4.
20	10	45	0.	0.	0.
21	11	0	0.	0.	4.
22	11	45	0.	0.	0.

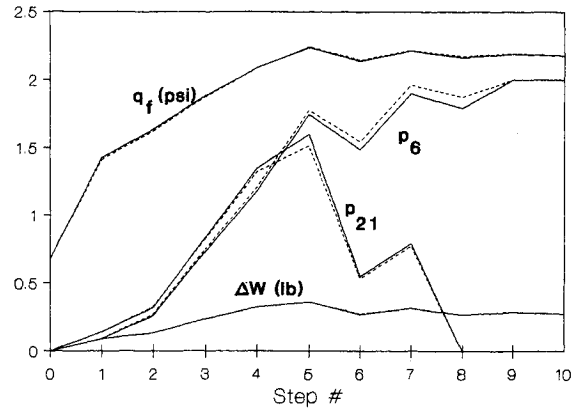

Fig. 6 Variations of flutter dynamic pressure, added weight, and two structural variables along the optimization path, case III.

The variations of q_f, ΔW, and the typical p_{s6} and p_{s21} along the 10-step optimization process of case III are plotted in Fig. 6. This case has been performed with a reduced-size 34-state aeroservoelastic model (22 structural, 6 aerodynamic, and 6 control states). The computation cpu time was about 7 min on a MicroVax 3200. The dashed lines of Fig. 6 are for the same optimization process but with all the 25 data-base modes yielding a 62-state aeroservoelastic model, which took about 32 cpu min. The good agreement between the solid and dashed lines, and the associated cpu time differences demonstrate the accuracy and efficiency of the structural state reduction process.

Two NASTRAN model updates were performed with the final p_s values of cases III and IV of Table 5. The entire aeroservoelastic modeling process of Fig. 1 was repeated for each case, followed by root-locus stability analysis. All the new stability characteristics were within 3% of the associated ones in Table 4, which demonstrates the accuracy of the presented approach.

Conclusions

A systematic method for data-base construction, modeling, and structural and/or control optimization of aeroservoelastic systems has been presented. The method is applicable to any objective function that can be analyzed by the normal modes approach and analytically differentiated with respect to the design variables. Standard, commercially available finite element and unsteady aerodynamic computer codes can be used to construct the aeroelastic data base. Application of Mini-

mum-State rational approximations of the aerodynamic matrices yields a low number of aerodynamic states relative to the number of structural states. The weighting algorithm used to select modes for model size reduction, and the dynamic residualization method have been shown to yield high-accuracy, reduced-order models. The process of calculating the stability boundaries of the residualized system has been described, and the associated constrained sensitivity derivatives have been formulated. Expressions for an efficient calculation of aeroelastic effectiveness parameters and their sensitivity derivatives have been presented and used to implement aircraft performance requirements. The numerical applications demonstrated that, once the data base is constructed, a variety of optimal parametric studies with different cost functions and design constraints can be performed in on-line sessions without returning to the finite element model. The ensemble of all these analytical and computational techniques yields an efficient, high-accuracy optimization process which can be used as a practical design tool of realistic modern aeronautical composite structures and control systems.

Acknowledgment

This research was supported by NASA Grant NAGW-1708.

References

[1]Livne, E., Schmit, L. A., and Friedman, P. P., "Towards Integrated Multidisciplinary Synthesis of Actively Controlled Fiber Composite Wings," *Journal of Aircraft*, Vol. 27, No. 12, 1990, pp. 979–992.

[2]Livne, E., Schmit, L. A., and Friedman, P. P., "Exploratory Design Studies Using an Integrated Multidiscipinary Synthesis Capability for Actively Controlled Composite Wings," 31st Structures, Structural Dynamics and Materials Conference, AIAA Paper 90-0953, Long Beach, CA, April 1990.

[3]Giles, G. L., "Equivalent Plate Analysis of Aircraft Wing Box Structures with General Planform Geometry," *Journal of Aircraft*, Vol. 23, No. 11, 1986, pp. 859–864.

[4]Karpel, M., "Reduced-Order Aeroelastic Models via Dynamic Residualization," *Journal of Aircraft*, Vol. 27, No. 5, 1990, pp. 449–455.

[5]Karpel, M., "Sensitivity Derivatives of Flutter Characteristics and Stability Margins for Aeroservoelastic Design," *Journal of Aircraft*, Vol. 27, No. 4, 1990, pp. 368–375.

[6]Karpel, M., "Efficient Vibration Mode Analysis of Aircraft with Multiple External Store Configurations," *Journal of Aircraft*, Vol. 25, No. 8, 1988, pp. 747–751.

[7]Tiffany, S. H., and Adams, W. M., Jr., "Nonlinear Programming Extensions to Rational Approximation Methods of Unsteady Aerodynamic Forces," NASA TP-2776, July 1988.

[8]Karpel, M., "Design for Active and Passive Flutter Suppression and Gust Alleviation," NASA CR-3482, Nov. 1981.

[9]Karpel, M., "Time-Domain Aeroservoelastic Modeling Using Weighted Unsteady Aerodynamic Forces," *Journal of Guidance, Control, and Dynamics*, Vol. 13, No. 1, 1990, pp. 30–37.

[10]Karpel, M., and Hoadley, S. T., "Physically Weighted Approximations of Unsteady Aerodynamic Forces Using the Minimum-State Method," NASA TP-3025, March 1991.

[11]Hoadley, S. T., and Karpel, M. "Application of Aeroservoelastic Modeling Using Minimum-State Unsteady Aerodynamic Approximations," *Journal of Guidance, Control, and Dynamics*, Vol. 14, No. 6, 1991, pp. 1267–1276.

[12]Karpel, M., "Extensions of the Minimum-State Aeroelastic Modeling Method," *AIAA Journal*, Vol. 29, No. 11, pp. 2007–2009.

[13]Rodden, W. P. (ed.), "MSC/NASTRAN Handbook for Aeroelastic Analysis," MacNeal-Schwendler, Rept. MSR-57, Los Angeles, CA, Nov. 1987.

[14]Karpel, M., and Sheena, Z., "Structural Optimization for Aeroelastic Control Effectiveness," *Journal of Aircraft*, Vol. 26, No. 5, 1989, pp. 493–495.

[15]Haftka, R. T., Gurdal, Z., and Kamat, M. P., "Constrained Optimization," *Elements of Structural Optimization*, 2nd ed., Kluwer Academic Publishers, The Netherlands, 1990, pp. 135–176.